



UNIVERSITY OF LEEDS

This is a repository copy of *Modeling the Altitude Distribution of Meteor Head Echoes Observed with HPLA Radars-Implications on the Radar Detectability of Meteoroid Populations*.

White Rose Research Online URL for this paper:
<http://eprints.whiterose.ac.uk/143454/>

Version: Published Version

Article:

Swarnalingam, N, Janches, D, Carrillo Sanchez, JD et al. (4 more authors) (2019) Modeling the Altitude Distribution of Meteor Head Echoes Observed with HPLA Radars-Implications on the Radar Detectability of Meteoroid Populations. *Astrophysical Journal*, 157 (5). 179. ISSN 0004-637X

<https://doi.org/10.3847/1538-3881/ab0ec6>

© 2019 The American Astronomical Society. All rights reserved. This paper has been published in *Astrophysical Journal*. Uploaded in accordance with American Astronomical Society self-archiving policy.

Reuse

Items deposited in White Rose Research Online are protected by copyright, with all rights reserved unless indicated otherwise. They may be downloaded and/or printed for private study, or other acts as permitted by national copyright laws. The publisher or other rights holders may allow further reproduction and re-use of the full text version. This is indicated by the licence information on the White Rose Research Online record for the item.

Takedown





If you consider content in White Rose Research Online to be in breach of UK law, please notify us by emailing eprints@whiterose.ac.uk including the URL of the record and the reason for the withdrawal request.



eprints@whiterose.ac.uk
<https://eprints.whiterose.ac.uk/>



Modeling the Altitude Distribution of Meteor Head Echoes Observed with HPLA Radars: Implications for the Radar Detectability of Meteoroid Populations

N. Swarnalingam^{1,2} , D. Janches¹ , J. D. Carrillo-Sanchez³, P. Pokorný^{1,2} , J. M. C. Plane³ , Z. Sternovsky⁴, and D. Nesvorný⁵

¹NASA Goddard Space Flight Center, Greenbelt, MD, USA; nimalan.swarnalingam@nasa.gov

²Department of Physics, Catholic University of America, Washington, DC, USA

³School of Chemistry, University of Leeds, Leeds, UK

⁴Laboratory for Atmospheric and Space Physics, University of Colorado Boulder, Boulder, CO, USA

⁵SouthWest Research Institute, Boulder, CO, USA

Received 2018 August 30; revised 2019 January 23; accepted 2019 March 6; published 2019 April 17

Abstract

The altitude distribution of meteors detected by a radar is sensitive to the instrument's response function and can thus provide insight into the physical processes involved in radar measurements. This, in turn, can be used to determine the rate of ablation and ionization of the meteoroids and ultimately the input flux on Earth. In this work, we model the radar meteor head echo altitude distribution for three High Power and Large Aperture radar systems, by considering meteoroid populations from the main cometary family sources. In this simulation, we first use the results of a dynamical model of small meteoroids impacting Earth's upper atmosphere to model the incoming mass, velocity, and entry angular distributions. We then combine these with the Chemical Ablation Model and establish the meteoroid ionization rates as a function of mass, velocity, and entry angle in order to determine the altitude at which these radars should detect the produced meteors and the portion of produced meteors from each population that are detected by these radars. We explore different sizes of head plasma as well as the possible effects on radar scattering of the head echo aspect sensitivity. We find that the modeled altitude distributions are generally in good agreement with measurements, particularly for ultra-high-frequency radars. In addition, our results indicate that the number of particles from Jupiter Family Comets (JFCs) required to fit the observations is lower than predicted by astronomical models. It is not clear yet if this discrepancy is due to the overprediction of JFC meteoroids by dynamical models or due to unaccounted physical processes in the treatment of ablation, ionization, and detections of meteoroids as they pass through Earth's atmosphere.

Key words: atmospheric effects – instrumentation: detectors – meteorites, meteors, meteoroids – techniques: radar astronomy – techniques: radial velocities

1. Introduction

Each day, billions of meteoroids with masses smaller than a milligram enter Earth's atmosphere and ablate in the altitude range ~ 70 – 130 km. While they are responsible for the formation of metal layers and metal chemistry in the mesosphere and lower thermosphere (e.g., Plane et al. 2003), they also serve as condensation nuclei for the nucleation of mesospheric ice particles, which cause polar mesospheric clouds and polar mesospheric summer echoes (e.g., Rapp & Lübken 2004), as well as for the polar stratospheric cloud particles, which play a major role in the formation of the ozone hole (e.g., Voigt et al. 2005; James et al. 2018). The majority of these particles that reach Earth's atmosphere originate from the zodiacal cloud, which is a circumsolar disk pervading the space primarily between the Sun and Jupiter. While the particles in the zodiacal cloud originate from asteroid collisions, cometary activity and collisions in the inner solar system, and interstellar medium grains (e.g., Grim & Staubach 1996), the primary sources for submilligram particles are short-period Jupiter Family Comets (JFCs), long-period Halley-type Comets (HTCs), Oort Cloud Comets (OCCs), and particles from the asteroid belt (ASTs; e.g., Nesvorný et al. 2010; Pokorný et al. 2014; Janches et al. 2018).

For many years, ground-based and space-borne measurements, along with simulation and modeling efforts, have been actively conducted to understand the impact of these submilligram particles on Earth's atmosphere (e.g.,

Pellinen-Wannberg & Wannberg 1994; Close et al. 2000; Janches et al. 2000; Mathews et al. 2001; Chau & Woodman 2004; Close et al. 2004; Plane 2004; Jones et al. 2005; Campbell-Brown & Close 2007; Brown et al. 2008; Dyrud et al. 2008; Schult et al. 2013; Janches et al. 2014b). However, a great level of uncertainty remains in the estimation of the incoming flux among the different approaches (e.g., Plane 2012; Carrillo-Sánchez et al. 2016). As a result, the relative contributions of the primary sources in the incoming flux also remain debated quantities. For example, the zodiacal cloud model developed by Nesvorný et al. (2010) predicts that $\sim 85\%$ – 95% of the particles in the cloud are from JFCs. According to the authors, because most of the predicted JFCs impacting Earth are low-velocity particles, it is expected that they will not be detected by radars, due to the fact that they would not produce sufficient ionization during ablation in Earth's atmosphere. While this prediction is supported by two optical studies using observations of infrared emission from the zodiacal cloud by Rowan-Robinson & May (2013) and Yang & Ishiguro (2015), and also by a modeling study of the fluxes and Na and Fe atoms in Earth's upper mesosphere and the deposition rate of cosmic spherules at the surface by Carrillo-Sánchez et al. (2016), a series of studies utilizing High Power and Large Aperture (HPLA) radars together with the modeling effort by Janches et al. (2014b, 2015, 2017) argued that the dominance of these populations should be reflected in the observations of the most sensitive HPLA radars. This is not the

case; however, questions of why or how these particles could be undetected by sensitive radars remain unanswered.

While previously we have focused on modeling the detected rate and velocity distributions of meteors (Janches et al. 2014b, 2015, 2017), in this study we focus on modeling the observed altitude distribution of meteors by three HPLA radars, which ultimately describes the radar response function, thereby providing confidence in our treatment of where meteoroids ablate and produce sufficient ionization for their detection. Two Ultra High Frequency (UHF) systems and a Very High Frequency (VHF) system are utilized in this work. They are the 430 MHz Arecibo Observatory’s radar located in Puerto Rico (18°N, 67°W), the 450 MHz Poker Flat Incoherent Scatter Radar (PFISR) located near Fairbanks in Alaska (65°N, 147°W), and the 46.5 MHz Middle and Upper Atmosphere (MU) radar located at Shigaraki in Japan (35°N, 136°E). We use a combination of dynamical models of various meteoroid populations, reported by Nesvorný et al. (2010, 2011a) for the case of JFCs, Pokorný et al. (2014) for the case of HTC’s, and Nesvorný et al. (2011b) for the case of OCCs along with an ablation model (Vondrak et al. 2008) and radar detection model to determine what portion of the incoming population is detected by the particular radar as a function of meteoroid mass, velocity, and entry angle, following the work by Janches et al. (2014b, 2015, 2017). Finally, we introduce a Monte Carlo treatment to model the altitude distribution and test the results for different physical parameters of the produced head echoes.

2. Methodology

2.1. Meteor Ablation and Radar Scattering

When a meteoroid travels through the atmosphere, it loses its momentum and energy due to collisions with air molecules resulting in an increase of the temperature of both the meteoroid and the impinging air. Ablated meteor atoms and atmospheric constituents that have collided form a high-density plasma vapor cloud immediately surrounding the meteoroid moving along at or near its speed (e.g., Mathews et al. 1997; Janches et al. 2000; Close et al. 2002). This plasma region or head plasma is significantly smaller than the more common meteor trail, and thus usually requires high power and greater system sensitivity, via a large antenna aperture, in order to be detected as a head echo (e.g., Janches et al. 2014a). Over the years, several theoretical and experimental studies have been actively conducted on head echoes, and those studies provided extensive information about the electromagnetic interactions in the meteor plasma (Close et al. 2002, 2004; Chau & Woodman 2004; Mathews 2004; Janches et al. 2008; Kero et al. 2012; Marshall & Close 2015; Oppenheim & Dimant 2015; Dimant & Oppenheim 2017a, 2017b, and several others). Nevertheless, uncertainties still exist, especially with respect to the nature of the scattering mechanism responsible for the head echoes.

In this study, we capitalize on the head echo radar detection model reported by Janches et al. (2014b, 2015, 2017) and expand it to model the altitude distributions of these HPLA radar head echo observations. We consider meteoroids with masses in the range of 0.01–1000 μg , entry velocities between 11 and 72 km s^{-1} , and zenith entry angles between 0° and 90°. The velocity range considered in this work represents the bulk of meteors detected by radars, and we do not consider the rarer events with velocity higher than 72 km s^{-1} , which represent

hyperbolic orbits. We also utilize the Chemical Ablation MODel (CABMOD; Vondrak et al. 2008) to estimate the meteor ionization and ablation. Our model does not predict any detection above 130 km for the chosen meteoroid mass, velocity, and entry angle ranges, which agrees with the bulk of the HPLA detections. However, observations of rare events above 130 km have been reported (e.g., Gao & Mathews 2015a, 2015b and references therein), and these studies have suggested that such high-altitude events are due to sputtering (e.g., Popova et al. 2007). CABMOD includes sputtering at high altitude using a semiempirical formalism derived from laboratory studies of ion sputtering, and this is reasonable within an order of magnitude. The model showed that sputtering is responsible for the ablation above the height where the particle melts and the rate of sputtering then decreases exponentially with height (following the decrease of atmospheric density). For example, the sputtering rate at ~ 120 km is about 5 orders lower than the peak of ablation below 90 km. At ~ 150 km, the rate will be about 7 orders of magnitude lower than the peak (Vondrak et al. 2008). While sputtering may be relevant to large bodies producing fireballs or bolides observed optically, CABMOD’s physical treatment of this effect demonstrates that at least, to first order, this process is negligible for the size ranges of particles producing the HPLA meteor head echoes discussed in this work.

In our model, the scattering from the head echo is considered to arise from a volume of electrons that is small compared to the incident radar wavelength and thus it can be assumed that all electrons would scatter off in-phase radio waves to produce coherent backscattering (e.g., Mathews et al. 1997). Based on this assumption, the signal-to-noise ratio (S/N) of backscatter signals is given by

$$S/N = \frac{P_T \lambda^2 G^2 \sigma}{(4\pi)^3 P_N h^4}, \quad (1)$$

where P_T is the transmitted power, λ is the radar wavelength, G is the one-way antenna gain pattern, σ is the radar scatter cross section, h is the target range, and P_N is the radar system noise power, which is given by

$$P_N = k \Delta f T_{\text{sys}}, \quad (2)$$

where k is the Boltzmann constant, Δf is the noise bandwidth, and T_{sys} is the equivalent system temperature (e.g., Swarnalingam et al. 2009).

Generally, for the case of meteor detections using radars, two limiting cases of plasma densities—underdense and overdense—are considered. For the case of underdense meteor plasma, the electron density is sufficiently low to allow the incident wave to propagate along the plasma, and thus each individual electron will scatter independently. On the other hand, for the case of overdense meteor plasma, the electron density will be sufficiently large to totally reflect the incident wave. Mathews et al. (1997) reported a head echo model in which the scattering target was considered to be underdense, and thus the resulting backscatter signal is proportional to the number of electrons in the confined small volume. Later, Close et al. (2002) argued that the scattering strongly depends not only on the plasma density but also on the mean free path (MFP) of the atmospheric molecules. Subsequently, a cloud of electrons of a size comparable to the MFP of atmospheric molecules has been applied in several meteor head echo radar studies (e.g., Close et al. 2002; Westman et al. 2004; Janches et al. 2008).

Marshall & Close (2015) developed a three-dimensional Finite-difference Time-domain (FDTD) model to investigate the scattering of radar waves from meteor head echoes. Treating as a cold, collisional, magnetized plasma, they explored the dependence of the radar cross section (RCS) on physical variables such as the plasma density, meteor head echo scale sizes, and the radar wave frequency. These authors found that the computed RCS disagrees with a previous analytical theory at certain meteor head echo sizes and densities. They also concluded that for overdense meteors, the meteor head RCS is given by the overdense area of the meteor, defined as the cross-section area of the part of the meteor where the plasma frequency exceeds the wave frequency. In the case of underdense meteors, the model provides a monotonic relationship between the meteor plasma size and peak density, and the resulting RCS. These results provide a physical measure of the meteor head echo size and density that can be inferred from measured RCS values from ground-based radars. However, Janches et al. (2017) examined how well the simple head echo model reported by Mathews et al. (1997) compares with the more comprehensive FDTD model reported by Marshall & Close (2015). Janches et al. (2017) showed that the coherent scattering model utilized by our approach is in reasonably good agreement with the FDTD simulations for the range of masses between 0.01 and 1000 μg , where at low velocities the RCS from the FDTD simulations is at most a factor of 0.1 smaller than that resulting from the coherent scattering approach (see Figure 6 in Janches et al. 2017). The FDTD model assumes a Gaussian electron density distribution (Close et al. 2012), and from these results, it appears that coherent scattering works reasonably well as an approximation when the head echo is underdense. That is, the head plasma should emulate coherent scattering as the radar wave is able to penetrate the plasma and be seen by all of the head plasma electrons. The calculated electron densities from CABMOD result in normalized plasma frequencies that are smaller than 3 and actually generally smaller than 1. Thus, the relatively simple coherent scattering parameterization approximates reasonably well the results of the general FDTD model for the particular case of underdense head echoes, which applies to the range of dominant meteoroid masses and speeds utilized in this work. Therefore, the choice of the head echo scattering model used here is not expected to yield very different results, and thus we define the radar scatter cross section in our model as

$$\sigma = 4\pi r_e^2 \left(2n_e F \frac{r_{\text{MFP}}}{L} \right)^2, \quad (3)$$

where r_e is the classical electron radius (2.8179×10^{-15} m), n_e is the electron number density, and r_{MFP} is the atmospheric MFP. F is a factor (it will be defined shortly) and L is a parameter introduced in this work to characterize the size of the scattering volume of the head plasma. In order to produce coherent backscattering, the size of plasma must be smaller than the incident radar wavelength. When the plasma size is larger than a quarter of the radar wavelength, the strength of the electromagnetic signals that penetrate the plasma will decrease, which can cause destructive interference (Janches et al. 2017). For the case of the 430 MHz Arecibo and 440 MHz PFISR radars, this transition would take place at ~ 100 km altitude (i.e., $r_{\text{MFP}} = 0.17$ m). For the case of the 46 MHz MU radar, it will occur at ~ 112 km altitude (i.e., $r_{\text{MFP}} = 1.6$ m). In order to

accommodate this transition in the scattering volume, we include the factor F in our detection model, as defined by Janches et al. (2017):

$$F = \begin{cases} 1 & \text{if } \left(\frac{r_{\text{MFP}}}{L} \right) \leq \frac{\lambda}{4} \\ \left(\frac{\lambda}{4r_{\text{MFP}}} \right)^2 & \text{if } \left(\frac{r_{\text{MFP}}}{L} \right) > \frac{\lambda}{4}. \end{cases} \quad (4)$$

The factor F accounts for when the plasma size is larger than a quarter of the radar wavelength; this will reduce the scattering ability of the interior electrons. Although initially the radar scattering volumes were considered to be equal to a sphere of radius r_{MFP} (e.g., Janches et al. 2014b), it was argued by Close et al. (2004) that the head plasma must be smaller than r_{MFP} in order to match the ARPA Long-Range Tracking and Instrumentation Radar (ALTAIR) observations with their model. Following that work, Janches et al. (2017) applied a smaller scattering volume of size $r_{\text{MFP}}/5$, compared to the previously assumed size, arguing that the smaller plasma size could partially explain the expected lack of detection of slow moving meteoroids by these radars. We explore in this study how different values of L match the observation results.

2.2. Limitations in Head Echo Detection for Different Radar Systems

The sensitivity of the radar system depends on several parameters, including its design, transmitted peak power, antenna gain, antenna aperture, and receiver system temperature. In the case of the 46 MHz MU radar, the sky noise (galactic noise) also can affect the sensitivity in the detection of the backscattered signals, as it is most dominant at lower frequencies (Swarnalingam et al. 2009). In order to detect a meteor, the received backscattered signals from the head plasma must be higher than a system-dependent threshold. On the other hand, while inside the radar beam, the signal strength of a particular meteor depends on the rate of electron production during its ablation process and also on the size of the head plasma, which is, in turn, dependent on altitude. That is, if the meteoroid enters the radar beam at an altitude too early during the ablation process such that insufficient ablation and ionization have occurred, then there will not be enough electrons in the head plasma for the backscatter signal to exceed the detection threshold. Likewise, if the meteoroid enters the radar beam too late during the ablation process, most of the ionization will be spent, and once again, there will not be enough electrons to produce a detectable backscatter signal. As shown by Janches et al. (2014b, 2015), for a given meteoroid mass, velocity, and entry angle, there will be a confined altitude range in which the particle must enter the radar beam for detection to take place. This altitude range is not only dependent on meteoroid physical parameters but also on the radar system. Thus, by modeling accurately these altitude ranges, which can be considered as a proxy of the radar response function, we can gain confidence in our treatment of the various physical parameters involved in the detection of these particles. Note that as described in Section 2.1, the meteoroid dynamical characteristic considered in this work includes the altitude ranges below 130 km.

In order to model the altitude distribution detected by each radar system, we expand on the work reported by Janches et al. (2017) and estimate the S/N profiles as a function of altitude

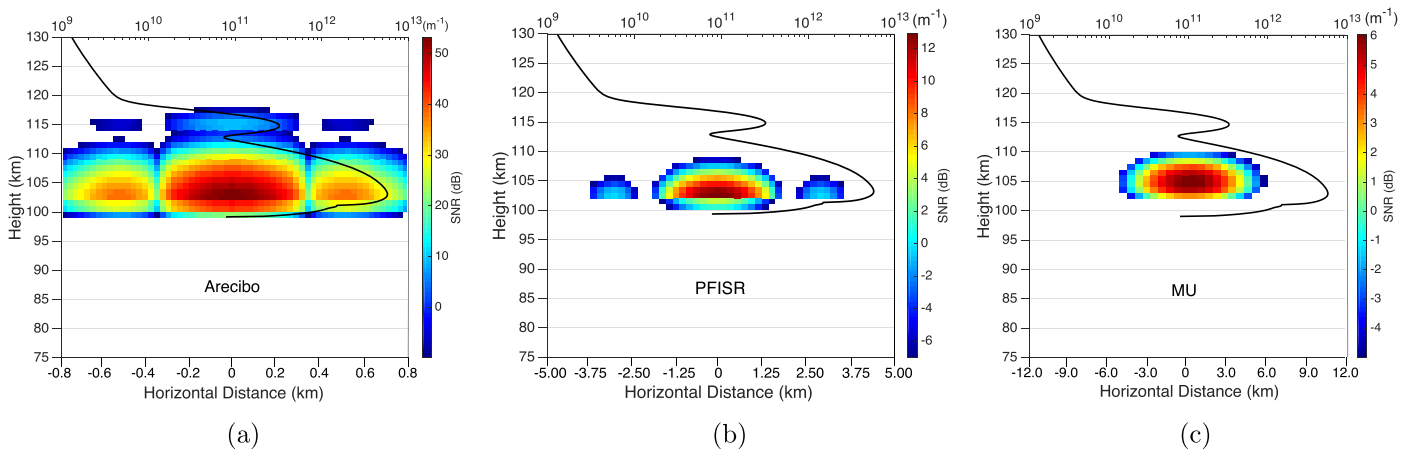


Figure 1. Altitude ranges for which the S/N is at detectable levels for the Arcsibo (panel a), PFISR (panel b) and MU (panel c) radars for the case of a meteoroid of mass $5 \mu\text{g}$ entering the atmosphere at 40° zenith angle with a velocity of 56 km s^{-1} . The black line represents the altitude profile of the electron number density (m^{-1}) predicted by CABMOD. The meteor will be detected by the radar only if it enters the radar beam at altitudes within the respective ranges. For this example, the Arcsibo radar has a more extended range, which includes the ablation of alkalis such as Na and K (~ 112 – 118 km) as well as the main constituents such as Si, Mg, and Fe; the other two radars can detect the meteor only during the ablation of the main constituents. Radar beam cross sections include the first sidelobes. Horizontal distances are estimated at 100 km altitude.

and meteoroid dynamical and physical parameters for each radar system utilizing the CABMOD. It takes into account the momentum and energy balance for micrometeoroids entering Earth’s atmosphere with a given velocity and entry angle, and predicts ablation regimes as a function of mass, velocity, and entry angle for various ablated metallic atoms and electrons (Vondrak et al. 2008). The model treats meteoroids with masses in the range of 0.01 – $1000 \mu\text{g}$, entry velocities between 11 and 72 km s^{-1} , and zenith entry angles between 0° and 90° . CABMOD uses meteoroid composition formed by eight molten oxides— Na_2O , K_2O , FeO , SiO_2 , MgO , Al_2O_3 , TiO_2 , and CaO —and predicts mainly two altitude regimes for their ablations. The first one is a rapid and narrow height region produced by the ablation of the alkali elements Na and K, and the second regime occurs at lower altitudes over a wider altitude range produced by the ablation of the main elements such as Si, Mg, and Fe. Recently, the model was further refined based on two laboratory experiments: measurement of the ionization coefficient in the meteor ablation process using iron particles impacting N_2 , CO_2 , and He gases and air by Thomas et al. (2016), and measurements of the ablation rates of Na, Fe, and Ca by Gómez Martín et al. (2017). The updated version of CABMOD predicts an extended altitude range of electron production for the case of the ablation of alkalis as compared to the original model. In addition, the resulting altitude of the peak electron production due to the ablation of the main meteoroid constituents is decreased by 1 – 2 km to lower altitudes compared to the earlier version (Janches et al. 2017).

Similar to Janches et al. (2017), we use electron altitude profiles obtained with the updated version of CABMOD to estimate the S/N altitude profiles for the Arcsibo, PFISR, and MU radars as a function of mass, entry velocity, and entry zenith angle. Figure 1 shows the altitude ranges at which the produced signal is predicted to become detectable for each radar utilized in this study for the case of a $5 \mu\text{g}$ meteoroid entering the atmosphere at 40° zenith angle with a velocity of 56 km s^{-1} for Arcsibo (panel a), PFISR (panel b), and MU (panel c). The black line represents the electron number density altitude profile (m^{-1}) for this meteor ablation predicted by the updated version of CABMOD. As is shown in Figure 1 and also described in Janches et al. (2014b), if the meteoroid enters

the radar beam at altitudes either higher or lower than the ranges shown, it will not be detected by the respective radar system. As expected, because the Arcsibo radar sensitivity is much higher than that of the other systems for this particular case, it has an extended altitude range in which the detection is possible as compared to the other systems. In addition, the Arcsibo radar can detect electrons produced by the ablation of both alkalis as well as the main elements even for such a small meteor. However, for the relatively less sensitive PFISR and MU radars, the detectable altitude ranges are narrower, and they are only able to detect electrons produced by the ablation of the main constituents.

2.3. Determination of Altitude Distributions at Different Radars

To determine the velocity, mass, and entry direction of each meteor, we utilize dynamical models that consider populations of the principal meteoroid sources forming the zodiacal cloud. These combine with the location of each radar along with the temporal and geographical variability of the meteoric input (referred to as the Meteor Input function or MIF). We include short-period JFC particles as well as particles from long-period HTC and OCCs. We do not consider main belt asteroidal particles because they will not produce sufficient ionization to be observed by radars, due to their very low geocentric velocity. JFC particles give rise to sporadic helion and antihelion meteoroid sources in the Sun-centered ecliptic coordinates. HTC and OCC particles give rise to the north and south apex sources, and HTC particles also contribute to the north and south toroidal (NT/ST) sources. It is believed that JFC meteoroids dominate the mass influx to Earth (Nesvorný et al. 2010, 2011a; Carrillo-Sánchez et al. 2016). Each of these populations has dynamical properties characteristic of their origin (e.g., Janches et al. 2018). In particular for this work, their geocentric velocity distribution is more important. In addition, because each source has a unique radiant distribution, their diurnal variability and seasonality with respect to a ground-based observer also vary (Janches et al. 2006; Fentzke et al. 2009). However, studies show that seasonal variations in the observed altitude distributions are

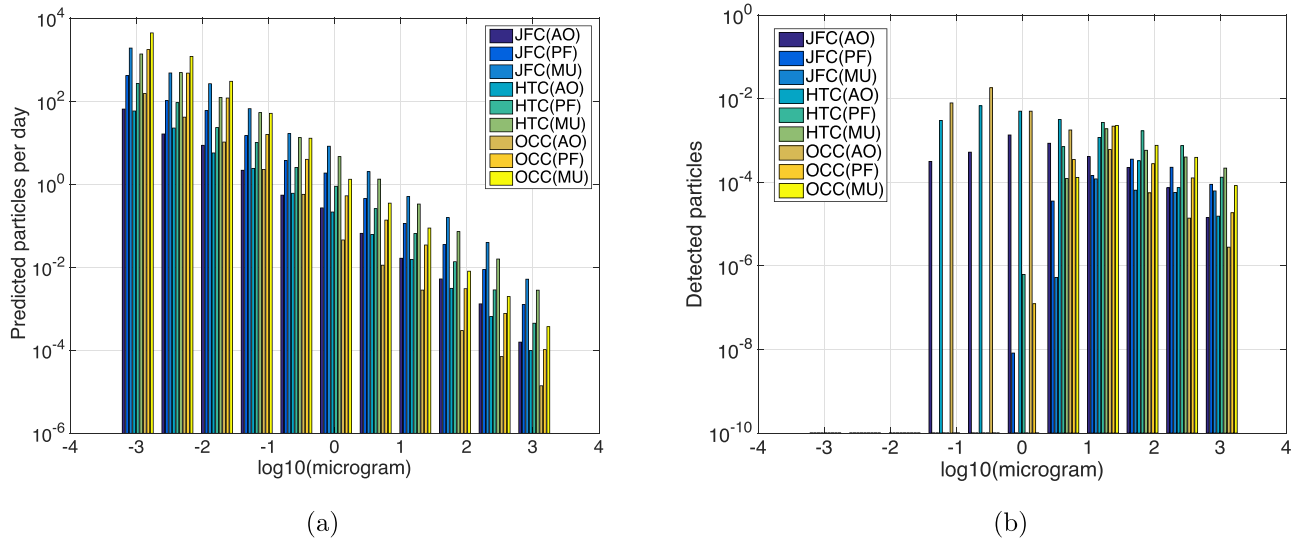


Figure 2. Histograms for mass distributions for JFCs, HTCs, and OCCs at the Arecibo (AO), PFISR (PF), and MU radars. Panel (a) shows the number of particles within the radar’s collecting area at each radar location predicted by the astronomical models. For each meteor source in these distributions, 1 metric ton mass per day over the entire planet is considered. Panel (b) shows the number of particles that will be detected by the respective radar system when the detection model described in Janches et al. (2017) is applied.

only dominant at high latitudes (e.g., Pifko et al. 2013; Schult et al. 2017). In our case, only PFISR is located at high latitude, and observations have shown seasonal variability in the altitude distribution (Sparks & Janches 2009a, 2009b). In order to avoid any potential bias between modeled and measured altitude distributions, due to different geographical locations and seasonal effects, we use atmospheric parameters obtained from the MSIS-E-90 Atmosphere Model (Hedin 1991; https://ccmc.gsfc.nasa.gov/modelweb/models/msis_vitmo.php) for the same geographical locations of the radar sites as well as for the same month in which the radar measurements were conducted. This allows us to match the radar measurements with the respective model.

We use mass distributions of JFC, HTC, and OCC particles. For each source, we consider 11 bins of masses in the range of 0.01–1000 μg , which have an assumed size–frequency distribution index equal to 4 (Carrillo-Sánchez et al. 2016; Pokorný et al. 2018). The dynamical evolution of these meteoroids follows the results reported by Nesvorný et al. (2011a) for JFCs, Pokorný et al. (2014) for HTCs, and Nesvorný et al. (2011b) for OCCs, along with the extension of these original models reported by Janches et al. (2018) and Pokorný et al. (2018). JFCs and HTCs have diameters in the range of 10–2000 μm , and OCCs have diameters in the range of 10–1200 μm (Pokorný et al. 2018). For each bin, we apply a correction factor that accounts for the detectability of particles by the particular radar as a function of their mass, velocity, and entry angle derived from the model reported by Janches et al. (2017). This correction or weighting factor represents the portion of incoming particles detected by each radar as a function of their dynamical characteristics. Figure 2 shows the mass distributions of these meteoroid sources. Panel (a) shows the number of particles independently predicted by these dynamical models to occur at the top of the atmosphere within each radar’s collecting area if they are detected. For each source, a normalized meteoroid mass input rate of 1 metric ton per day over the entire planet is considered. Panel (b) shows the predicted detection rate resulting from applying the correction factor derived from the radar detection model reported in

Janches et al. (2017). It can be seen from Figure 2(b) that there is a significant decrease in the number of particles, particularly for masses smaller than $\sim 0.065 \mu\text{g}$ as these meteors will not be detected by the radars due to the lack of sufficient ionization. In addition, the MU radar shows a relatively high number of detections for the case of higher masses of OCCs in comparison to the more sensitive Arecibo and PFISR. This is because the MU radar has a wider beam compared to Arecibo, and hence it is able to capture more of these less frequent particles than Arecibo. Nevertheless, this is only possible for the higher masses, due to the limitation in the detection sensitivity of this radar system.

Figure 3 shows the velocity distributions of JFCs, HTCs, and OCCs predicted to be detected by our model by applying again the correction factor derived from the detection model described in Janches et al. (2017) to each radar system. As expected, the number of particles detected by the Arecibo radar is higher for all populations compared to the other two radars, due to the fact that the distribution is dominated by the more frequent lower mass particles.

In order to determine the altitude distribution, we apply a Monte Carlo procedure. As described, we first estimate the weighted number of particles (i.e., the portion of particles that are predicted by our model as detectable particles) for meteors given their mass, entry velocity, and entry angle. For each meteor of specific mass, entry velocity, and entry angle, we obtain the altitude range where the radar can detect it using our radar detection model described earlier (see Figure 1). In order to determine the altitude at which each meteor is detected, we choose a number of random altitudes within this altitude range equal to the number of detected particles, given their mass, entry velocity, and entry angle. We consider this altitude to be the initial altitude at which each meteor is detected. Figure 4 shows the resulting altitude distributions of JFCs, HTCs, and OCCs for the three radars considered. For comparison purposes, all distributions in Figure 4 are normalized to the maximum of the resulting altitude distribution of OCCs modeled at the Arecibo radar. As can be seen in Figure 4, the dominant sources of particles that are detected by all three

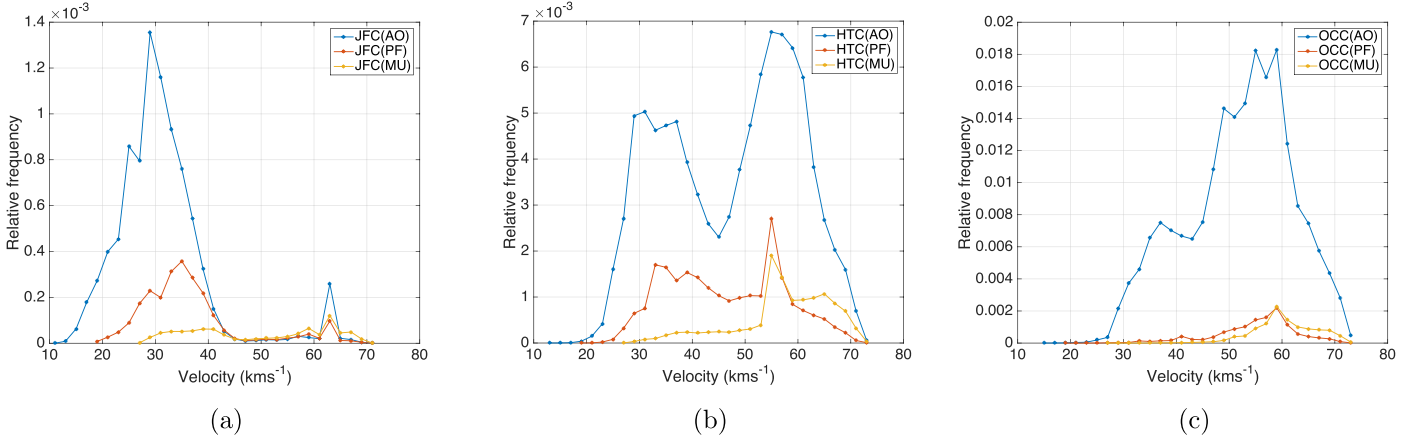


Figure 3. Comparison of weighted velocity distributions of JFCs, HTCs, and OCCs, predicted to be detected by the Arecibo (AO), PFISR (PF), and MU radars when the detection model described in Janches et al. (2017) is applied to each radar.

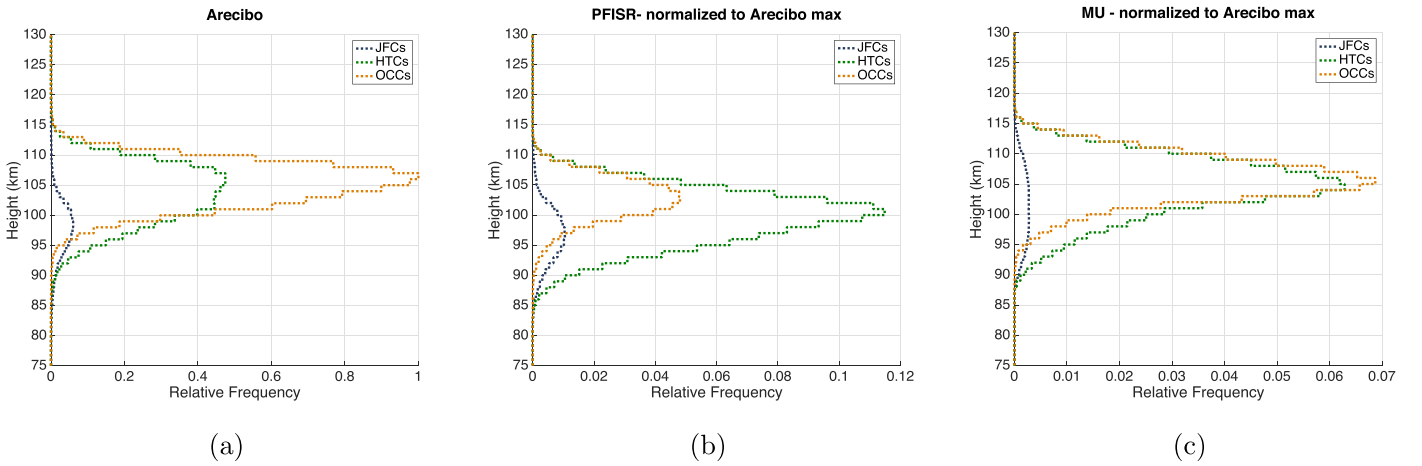


Figure 4. The altitude distributions for JFCs, HTCs, and OCCs from our model. For comparison purposes, all distributions are normalized to the maximum of the OCCs at the Arecibo radar.

radars are meteoroids from long-period comets (i.e., both HTCs and OCCs), and very few are from short-period JFCs. In addition, the JFC distribution peaks between 95 and 100 km both for Arecibo and PFISR, which is about 6–8 km lower than the peak of HTCs and OCCs. This could be due to the fact that the vast majority of low-mass and low-velocity JFCs tend to ablate at relatively low altitudes compared to HTCs and OCCs. On the other hand, such a difference is not as evident for the case of the MU radar simulation.

3. Comparison between Modeled and Observed Altitude Distributions

The MU radar has interferometric capability; hence, it can possibly distinguish the radiant from which each meteor detection originates (Kero et al. 2012; Pifko et al. 2013) and thus associate it with one of the three populations. However, both the Arecibo and PFISR observations were performed without interferometric capabilities, and hence it is not possible to distinguish the radiant of each individual meteor event at these two radars. Therefore, in order to compare our modeled altitude distributions with radar measurements, we combine the modeled distributions of the three meteoroid sources considered in this work. For this, we use a similar approach to that of Carrillo-Sánchez et al. (2016) and estimate the total altitude distribution Φ_{Tot} by combining the individual modeled

distributions of JFCs, HTCs, and OCCs as

$$\Phi_{\text{Tot}} = \alpha\Phi_{\text{JFC}} + \beta\Phi_{\text{HTC}} + \gamma\Phi_{\text{OCC}}, \quad (5)$$

where Φ_{JFC} , Φ_{HTC} , and Φ_{OCC} are the individual altitude distributions of each source, and the parameters α , β , and γ are the weighting coefficients representing the contribution of each population to the total altitude distribution. We adjust these coefficients to obtain an optimal fitting between our modeled altitude distribution and the radar measurements by applying a least-squares fitting procedure. We perform this procedure separately for each radar.

The range of coefficients used in the fitting procedure and the quality of their resulting fit are shown in Figure 5. The contour plots in the upper panel show the reciprocal of the sum of squared residuals for the coefficients α and $(\beta + \gamma)$, where the higher the values are, the better the fit is. It can be inferred from these contour plots that the optimal fitting for the $\alpha:(\beta + \gamma)$ ratio occurs at 0.50:1.00 for the Arecibo radar, at 5.80:2.70 for the PFISR, and at 38.0:8.00 for the MU radar. The lower panels of Figure 5 show the comparison between the modeled and measured altitude distribution in terms of absolute detected particle numbers per observing period for each radar. The black line represents the radar measurements, and the blue dotted line represents the best fit obtained from the fitting methodology described above.

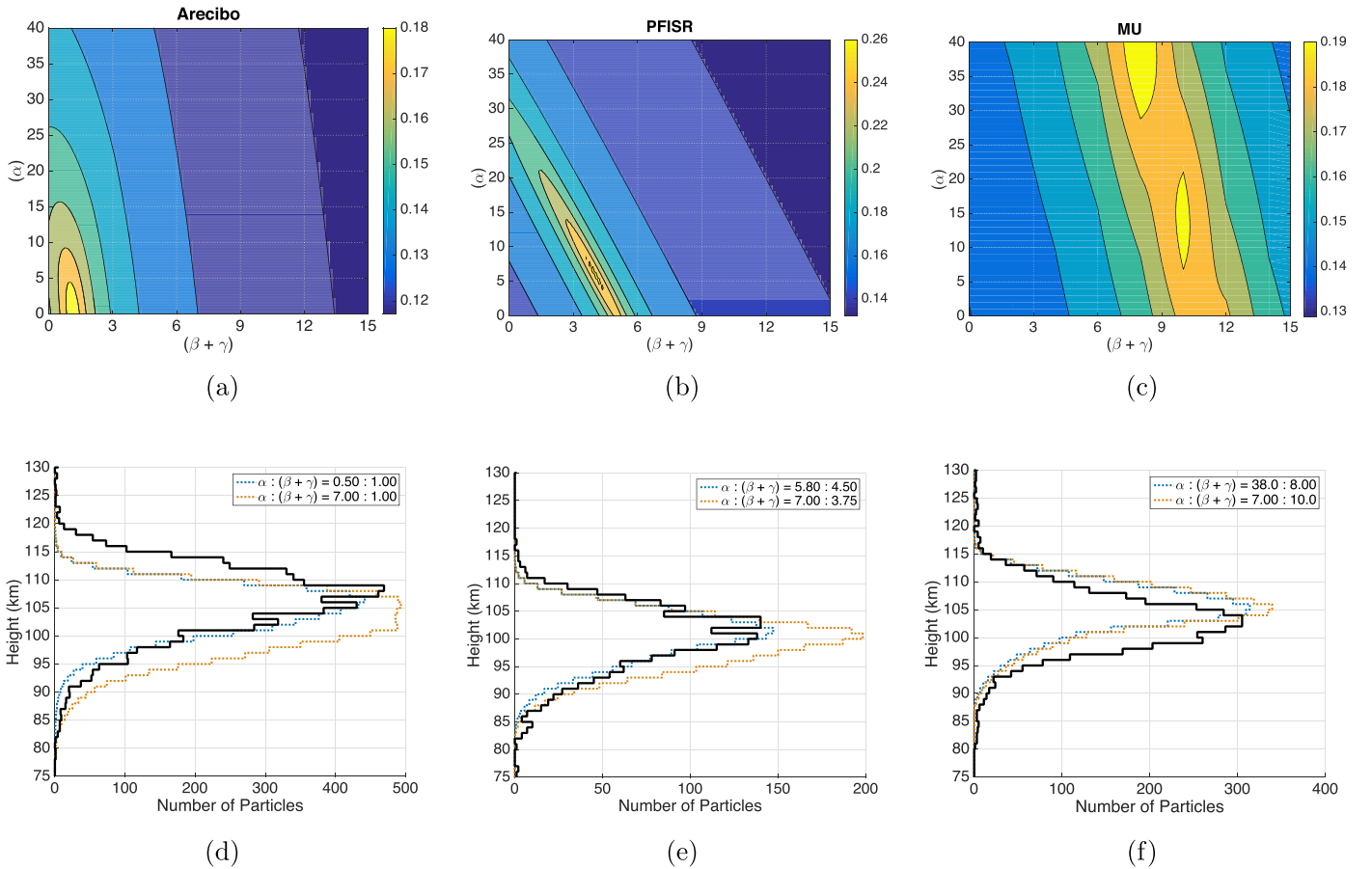


Figure 5. Upper panels: the contour plots for the solution space of α and $(\beta + \gamma)$ pairs for the fitting of modeled altitude distribution to radar measurements for the case of $L = 5$. The reciprocal of the sum of squared residuals for the coefficients are shown. Lower panels: a comparison of the modeled altitude distributions to the actual measurements (black lines) with two different sets of fitting coefficients. The blue dotted lines represent optimal fits, and the red lines represent fits in which a larger (for UHF radars) and smaller (for the MU radar) contribution of JFCs are used (see text for details).

Our model agrees reasonably well with the radar measurements for the case of Arecibo and PFISR. However, the estimated contribution from JFC particles is much smaller than the expected influx from other studies (e.g., Nesvorný et al. 2010; Carrillo-Sánchez et al. 2016), which required inputs of the order of 5–7 times larger than that from the long-period comets and meteoroids. Note that in this study, the coefficients α , β , and γ are scaling the number of particles whereas in the Carrillo-Sánchez et al. (2016) model, they scale the mass input. However, when considering the entire solution space, the contour plots in the upper panels of Figure 5 show that the α and $(\beta + \gamma)$ pairs allow for possible solutions in which the JFC contribution is dominant. We explore these values of α and $(\beta + \gamma)$ represented by the red dotted lines in the lower panels of Figure 5. As can be seen in Figure 5 (panels d and e), a solution pair in which JFC contribution is larger ($\alpha = 7$) results in a modeled distribution with a peak at altitudes lower than those measured by the UHF radars. This is because the majority of JFC particles have smaller masses and low velocities and thus they will penetrate deeper in the atmosphere during the ablation process. This causes our modeled altitude distribution to deviate from measurements when the value of α is increased.

Another feature of these results is the lack of the higher altitude tail of meteors in our model present in the Arecibo radar measurements between 110 and 120 km (see Figure 5(d)). The source of this discrepancy is not yet understood, because it does not seem to be present in the PFISR results. One

possibility is that CABMOD may underpredict the ionization of very small particles. It may be also possible that a small amount of volatile material (H_2O and organics) ablates at these heights and produces sufficient ionization to be detected by the Arecibo radar, but not by other radars. The next version of CABMOD planned will incorporate organics and will enable this issue to be further explored in a future work. We will also discuss this point further with respect to the size of head plasma in Section 3.1.

For the case of the MU radar, the estimated ratio of the population contribution $\alpha:(\beta + \gamma)$ is 38.0:8.00, which is in closer agreement to the results reported by Carrillo-Sánchez et al. (2016). However, it can be noticed from Figure 5(f) that unlike for the case of the UHF radar, the model predicted an altitude distribution with a peak about 2–3 km higher than the observed one. Furthermore, the MU distributions do not appear to be as sensitive to the choice of JFC contribution as was the case for the UHF radar as seen by the near-identical result represented by the blue line ($\alpha = 38.0$ for JFCs) and the red line ($\alpha = 7.00$). This indicates that because the MU radar does not detect a significant portion of JFCs (see Figure 4(c)), the respective coefficient α does not cause any significant impact on the optimal fitting of our model to the measured altitude distribution. As discussed in Section 2.3, the MU radar is not sensitive enough to detect particles that are under $20 \mu\text{g}$, and a large portion of JFC populations have masses lower than this threshold. This may indicate that the simple scattering model

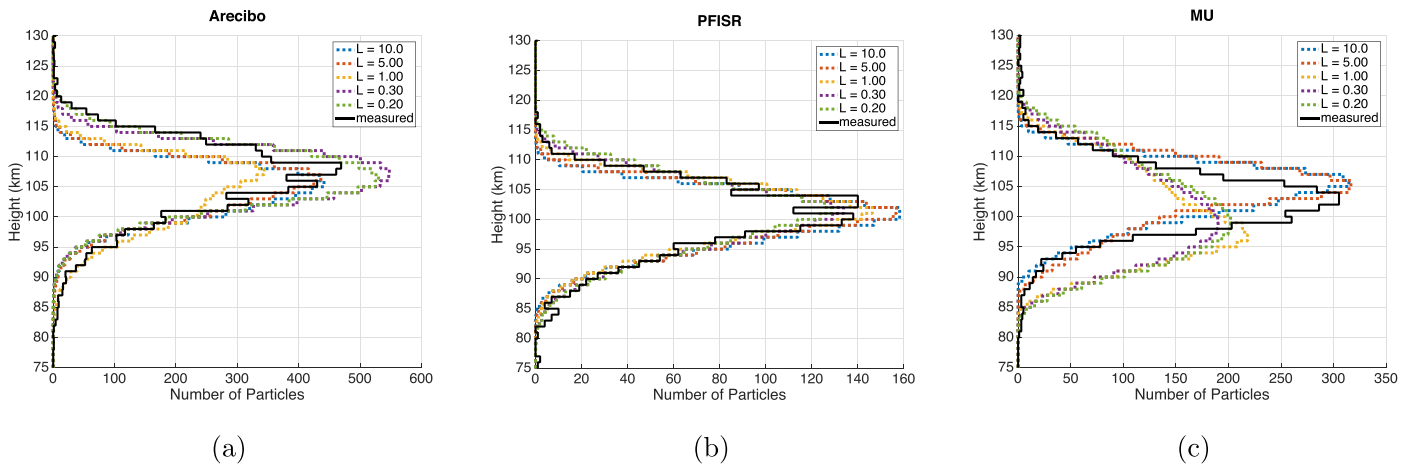


Figure 6. Comparison of the modeled altitude distributions, individually fitted to the measurements resulting from each radar at different head plasma sizes $L = 10, 5, 1, 0.3,$ and 0.2 . The solid thick black line represents the measured altitude distributions.

used in this work is not as applicable to VHF frequencies because the scattering is frequency-dependent (Close et al. 2004). Furthermore, the MU radar has a wavelength of ~ 6 m, which is significantly larger than the wavelengths of UHF radars (~ 0.7 m). The size of the head plasma may also play a role here. We will discuss this point further in the following section.

3.1. Size of the Radar Scatter Volume

The size of the head plasma responsible for the scattering of the radar signal is also an unknown quantity and critical in understanding the detectability of meteor head echoes (e.g., Marshall & Close 2015; Janches et al. 2017). As described in Section 2.1, we introduced the factor L in Equation (3) as a proxy of this physical parameter. In the previous sections, we have considered this factor to be $L = 5$ for all radars following the results reported in Janches et al. (2017). As seen in Figures 5(d) and (e), for the case of the UHF radars, $L = 5$ results in a good agreement for the case of PFISR, whereas for the case of the Arecibo radar, some differences can be observed at higher altitudes. As reported earlier, while the peak and lower portion of the Arecibo distribution are well reproduced, the model fails at reproducing the higher portion of the altitude distribution (particles between 110 and 120 km; see Figure 5(d)). We explore the impact that the radar scatter volume may have on the modeled distributions.

Figure 6 compares the modeled altitude distributions obtained using different radar scatter volumes with the following scale factors— $L = 10, 5, 1, 0.3,$ and 0.2 —with the measurements. For each choice of L , our modeled altitude distribution is individually fitted to the measurement. It can be seen from panel (b) in Figure 6 that there are no noticeable differences between the different L for the case of the distributions at PFISR, however some differences are observable for the case of Arecibo and MU radars (panels a and c, respectively). In the case of the Arecibo radar, larger scattering targets represented by $L = 0.3$ and 0.2 populate the high-altitude population that was previously missing while maintaining the peak of the distribution. This is because the head plasma size is larger than the atmospheric MFP, and thus, meteoroids would start being detectable at higher altitudes. This however deepens the conflict with the detectability of small and slow JFC meteors, which have been argued to not

produce enough ionization and thus remain undetected by radars (Nesvorný et al. 2010; Janches et al. 2014b). Janches et al. (2017) demonstrated that, at least for the case of Arecibo, this could happen when the head plasma is small. For the case of $L = 0.3$ and 0.2 , this would make these particles extremely detectable, and thus the radar observations should be dominated by JFCs, which is not the case. It is also worth noting that the size of the head plasma is being used here as a proxy to understand the causes of the differences between model and measurements. As the resulting lack of high-altitude meteors in the modeled Arecibo distribution is mostly associated with small particles, it is also possible that the CABMOD description of the ionization for the smaller sizes is underpredicted, possibly due to the early evaporation of organics and H_2O as mentioned earlier. Additionally, the quality of the modeled distributions at the MU radar somewhat agrees with the measurement for the case $L = 10$ and 5 , except for the 2–3 km difference in the peak of the distribution. However, the modeled distribution shape and peak start to deviate when L becomes 1 or lower (i.e., the head plasma becomes larger).

Possible explanations for these differences may be the fact that the MU radar transmits at a wavelength ~ 6 m, which is significantly larger than the wavelengths of the other two radars. It is evident from Figure 6(c) that increasing the radar target size makes a significant shift in the peak altitude of the MU radar. Similar differences in the peak altitudes between VHF and UHF were already measured in the simultaneous radar observations by Close et al. (2004) and Westman et al. (2004). Westman et al. (2004) observed that the peak altitude of the 224 MHz VHF radar was ~ 6 km higher than the peak altitude of the 930 MHz UHF EISCAT radar. Although this specific radar is located at a high latitude, where seasonal variations are dominant as studies have shown, the observational results emphasize the fact that the head echo is frequency-dependent, aside from also depending on atmospheric density as well as meteoroid entry velocity and mass (Close et al. 2004; Pellinen-Wannberg 2005). In our model, radar wavelength plays a role in determining the radar target size via the parameter F once the ratio between MFP and L becomes comparable to a quarter of the radar wavelength, and this may not be adequate enough to treat this issue.

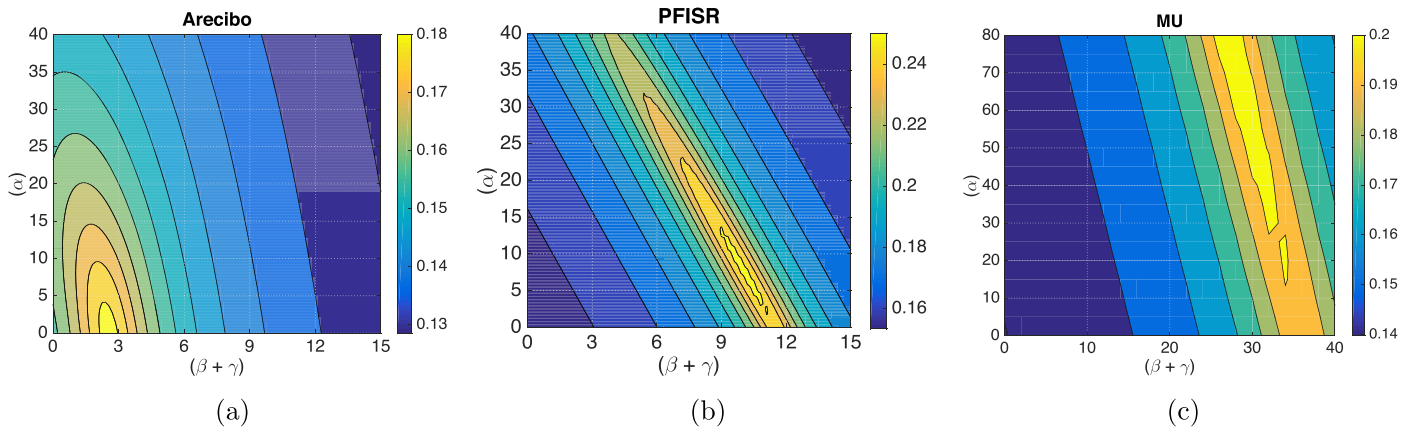


Figure 7. The contour plots for the solution space of α and $(\beta + \gamma)$ pairs for the fitting of modeled altitude distribution to radar measurements for the case $L = 10$.

Apart from this, because the detectability of the MU radar system is significantly lower compared to the other two systems (Janches et al. 2015, 2017), it cannot detect particles smaller than $20 \mu\text{g}$. Hence, a significant portion of JFCs is being left undetected by this radar. Therefore, it is possible that the MU radar actually observes a different portion of the mass distribution, in particular a higher mass range ($>1000 \mu\text{g}$) not included in CABMOD and this overall treatment. Not only do meteors with high masses tend to reach lower altitudes, they also have a high probability of fragmenting (Campbell-Brown & Jones 2003; Gao & Mathews 2015a; Subasinghe et al. 2016). This could add additional phenomena that need to be included in modeling radar measurements, in particular with the less sensitive MU radar.

Finally, Figure 6 also shows that the difference in the results utilizing $L = 10$ and 5 is negligible. Based on these facts, the choice of $L = 10$ and 5 makes our modeled altitude distributions fit reasonably well with the measurements in all three radars, in agreement with Janches et al. (2017). The choice of $L = 10$ would make the head plasma size smaller, thus it could increase the fitting coefficients. Figure 7 shows contour plots for the solution space of α and $(\beta + \gamma)$ for the case of $L = 10$. Comparing this with the upper panels of Figure 5, which represent the same for the case of $L = 5$, it is evident that the choice of $L = 10$ does not increase substantially the contribution of JFCs, especially at the UHF radars.

3.2. Impact Due to the Head Echo Aspect Sensitivity

The aspect sensitivity of the meteor head echo is the variation in the backscattered signal when the angle between the direction of the meteor vector velocity and the radar axis is nonzero. If the scattering mechanism is specular in nature, a decrease in the backscattered signal with the increase of this angle is observed. In such cases, the radar targets can no longer be assumed to be spherical scatterers. Instead, they are assumed to be on average oblate spheroids, with a Gaussian decrease in the electron density toward the edges (e.g., Hocking et al. 1986; Swarnalingam et al. 2011). Based on this, the polar diagram of the backscattered signal power $P_s(\theta)$ as a function of off-zenith entering angle θ is given by

$$P_s(\theta) = \exp\left(-\frac{\sin^2 \theta}{\sin^2 \theta_s}\right), \quad (6)$$

where the off-zenith angle θ_s is a measure for the aspect-sensitivity parameter (Swarnalingam et al. 2011). In the case of head echo observations, although the radar measurements are generally conducted using vertically directed beams, the aspect sensitivity could play a role, especially for meteors that have large entry angles. Janches et al. (2017) showed that this effect can be particularly important for the smaller particles detected by the Arecibo radar. In this section, we explore the role that the aspect sensitivity of meteor head echoes may have in the detectability and shape of the altitude distribution.

The influence of the aspect sensitivity on meteor head echo measurements has already been discussed in previous works (e.g., Janches et al. 2006, 2017; Fentzke & Janches 2008; Kero et al. 2008, 2012). In particular, using the EISCAT tristatic radar system, Kero et al. (2008) measured the S/Ns of a selected sample that occurs in the small common volume of the three receiving stations (Sodankyla, Tromso, and Kiruna) and thus could be observed from different angles. For this sample, which are produced by particles with sizes on the order of a millimeter, the authors showed that the head echo appears to be spherical and no aspect sensitivity was measured. However, more recently, Janches et al. (2017) argued that the aspect sensitivity mostly affects the Arecibo radar, and its effect would be negligible in other less sensitive radars. This is simply explained by the fact that because the Arecibo radar is highly sensitive, it detects the small and slow particles at the limit of ionization, and hence even a small angular effect would be enough to push the very weak backscattered S/Ns from these meteors below the radar’s detection threshold. While the detection of a meteor is highly dependent on what constituents are being boiled off, the authors showed that the ionization of these small and slow particles is very sensitive to small changes in velocity, mass, and potentially on angle, and these particles would never be detected by PFISR, MU, or the EISCAT tristatic system. In our model, in order to explore how this effect impacts the results, we incorporate a filtering effect in the backscattered powers. We implement this by combining Equation (6), which describes the reduction in the backscattered power for a range of entering angles for a choice of aspect-sensitivity parameter, θ_s , with Equation (1), which describes the S/Ns of the received powers. Therefore, the resultant aspect-sensitive-dependent S/N for received power

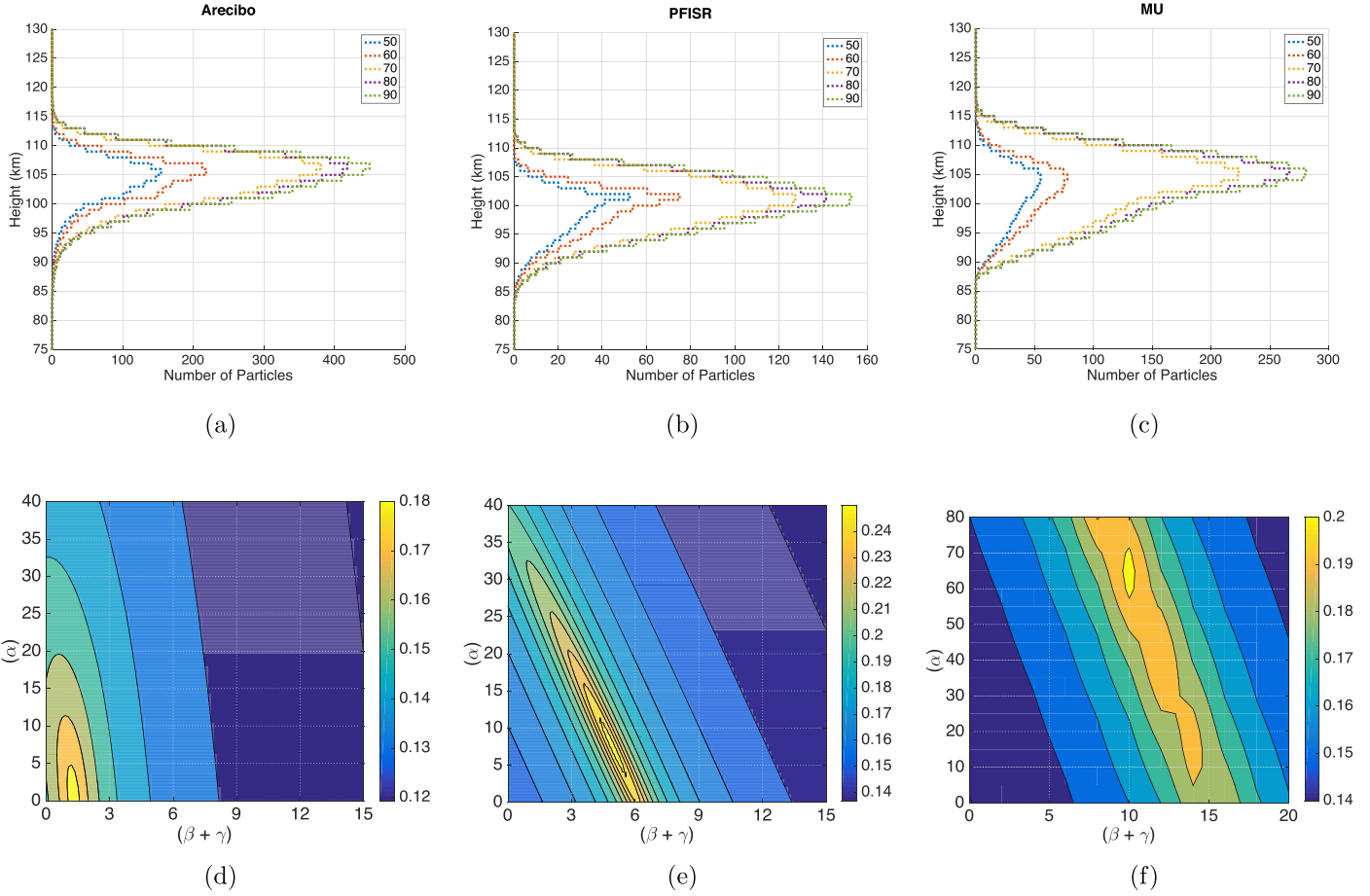


Figure 8. Upper panels: estimated altitude distributions for Arecibo, PFISR, and MU at different degrees of aspect sensitivity from $\theta_s = 50^\circ$ to 90° . The radar target volume sizes were set to 20% of the mean free path ($L = 5$). Lower panels: contour plots for the solution space of α and $(\beta + \gamma)$ pairs for the fitting of the modeled altitude distribution to radar measurements for the case $L = 5$ and $\theta_s = 70^\circ$.

can be written as

$$S/N(\theta, \theta_s) = \frac{P_T \lambda^2 G^2 \sigma}{(4\pi)^3 P_N h^4} \cdot \exp\left(-\frac{\sin^2 \theta}{\sin^2 \theta_s}\right). \quad (7)$$

From Equation (7), it can be seen that as the angle between the traveling direction of the meteor and the radar axis increases, the S/N will decrease. Figure 8 shows the results when this effect is accounted for in our model for the three radars. The upper panels show the altitude distributions for different values of θ_s . As expected, it can be observed in the upper panels that when the scatterers become more aspect-sensitive, the number of particles that are detected at each altitude is reduced without causing significant changes in the shape of the altitude distributions or in the height at which the peak occurs. More importantly, the reduction becomes significant only when θ_s becomes lower than 70° . The lower panels of Figure 8 show the contour plots for the solution space of α and $(\beta + \gamma)$ pairs for the best fits of our model to the respective radar measurements, similar to the plots shown in Figure 5, upper panels. For these results, we obtained the coefficients for the scatter volume size $L = 5$ by fitting the modeled altitude distribution for the particular case of $\theta_s = 70^\circ$ to the radar measurements, which is in agreement with the results reported by Fentzke & Janches (2008) and Janches et al. (2017). While applying the aspect sensitivity with $\theta_s = 70^\circ$ increases the values of the fitting coefficients at the two UHF radars, it makes very high coefficients in the case of the MU

radar. It can be inferred from Figure 8(f) that the best fit for the MU radar is obtained at $\alpha:(\beta + \gamma) = 65.0:10.0$. Therefore, we only use Arecibo and PFISR in this exercise because their similar frequencies but different sensitivities can shed light on how the different parts of the mass spectrum of the incoming flux are observed by these two radars.

Figure 9 describes the variations in the fitting coefficients α and $(\beta + \gamma)$ for the case of the Arecibo and PFISR radars as a function of the head echo aspect sensitivity for the ranges $\theta_s = 90^\circ$ to 50° . Panel (a) shows the dependence of α , which represents the contribution from JFCs, and panel (b) shows $(\beta + \gamma)$, which represents the contributions from HTC and OCCs. The coefficients α and $(\beta + \gamma)$ are estimated separately for each radar system by fitting the modeled altitude distribution for different values of θ_s to the measured altitude distribution of the respective radar scatter volume size $L = 5$. The blue (Arecibo) and black (PFISR) lines show the best fit for these coefficients, and the vertical bars indicate the 10% confidence level.

In the variation of the detectability of the aspect-sensitive micrometeoroid head echoes, it can be seen from Figure 9 that some agreement between both radars is found when $\theta_s = 70^\circ$ – 90° . It can be observed that when θ_s is decreased from 90° , the expected increments in the coefficients α and $(\beta + \gamma)$ due to aspect sensitivity are minimal up to $\theta_s = 70^\circ$. Although the coefficients start to increase when θ_s is reduced below 70° , the larger disagreement between the two radars also

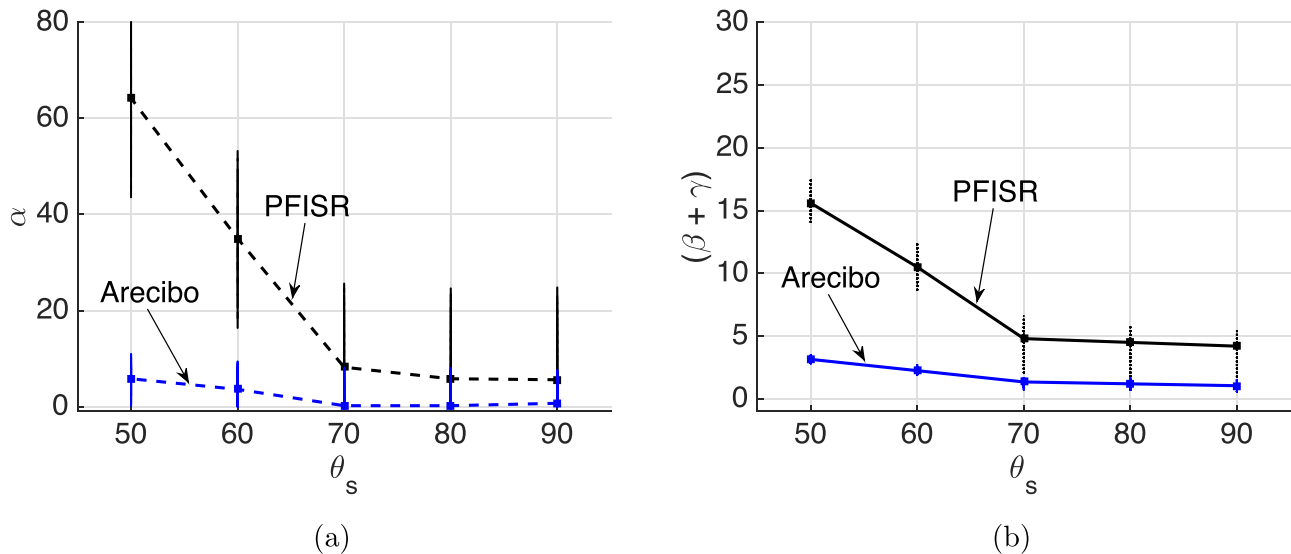


Figure 9. Variation of the fitting coefficients α (left) and $(\beta + \gamma)$ (right) with aspect-sensitivity angle for a head plasma scatter volume size $L = 5$ for Arecibo and PFISR.

increases. In the case of PFISR, the coefficient α , which represents the contribution required to fit the altitude distributions of JFCs, increases substantially to high values. It is important to remember that the Arecibo system has a greater detection sensitivity compared to PFISR, and this could explain the predicted high coefficients α and $(\beta + \gamma)$ for the case of PFISR. These results indicate that if the aspect sensitivity is present, it cannot be a strong effect, especially for a less sensitive radar such as PFISR. This conclusion is in agreement with the results reported by Janches et al. (2017) and not necessarily in disagreement with the measurements reported by Kero et al. (2008).

Earlier, in a simulation study of the meteor head plasma, Dyrud et al. (2008) found that the radar scatter cross section is significantly reduced at high aspect angles when the radar frequency is increased up to 300 MHz. Although the head plasma size considered by Dyrud et al. (2008) is much larger (\sim meters) than the size considered in our work (\sim centimeters), both results show good agreement. While these results show evidence that the aspect sensitivity of the head plasma reduces the radar detection of the meteors with increasing radar frequency, especially for higher aspect angles, it is not clear yet whether it is the aspect sensitivity or the radar detection sensitivity that plays the dominant role. Unfortunately in our case, because the UHF radars happen to have better detection sensitivities compared to the VHF radar, we are unable to verify this. However, the implementation of aspect sensitivity in our model increases the contribution of JFCs by a factor of 2–3 when $\theta_s < 70^\circ$.

4. Fitting a Single Solution for All Radars

In the previous sections, we treated the contributions of the various meteoroid sources contributing to the incoming meteor flux by fitting our model separately to each radar. However, the incoming flux should be independent of the instrument utilized to measure it, and so in this section we attempt to find a unique solution fitting simultaneously the observations of the three radars. That is, we apply the fitting procedure to obtain the best pair of coefficients α and $(\beta + \gamma)$ that will best describe the observations of the three radars simultaneously. We perform

this fit for the case of $\theta_s = 90^\circ$ and 70° , following the discussion presented in the previous section.

Figure 10 shows the results of fitting for these aspect angles. The upper panels show the altitude distributions for $\theta_s = 90^\circ$ (left) and 70° (right); the lower panels show the contour plots for the solution space of α and $(\beta + \gamma)$. As is shown in the upper panels, for the case of $\theta_s = 70^\circ$, the resulting fits are in good agreement with the observations obtained with the Arecibo radar, while for the case with no aspect-sensitivity effects, the model overpredicts the observations by $\sim 40\%$. For the case of the other radars, the unique solution underpredicts the observations and the aspect sensitivity does not improve the quality of the fitting. In both cases, the model underpredicts the observations by a factor of $\sim 60\%$ and 85% for PFISR and MU, respectively. As described above and shown also in Janches et al. (2017), the aspect-sensitivity effects appear to be important only for the smaller particles detected by the Arecibo radar compared to the other two radars. The best fit for all three radars is obtained for the ratio α and $(\beta + \gamma) = 1:1$ for the case $\theta_s = 90^\circ$ and α and $(\beta + \gamma) = 1.5:1$ for the case $\theta_s = 70^\circ$, which once again highlights the issues with detecting the low-velocity JFC meteoroids, which are allegedly the dominant portion of the incoming flux. With the current knowledge of meteor ablation, ionization, and radar detection included in our model, the results continue to suggest that if this large population exists, it should be detected by these sensitive radars. For the case of $\theta_s = 90^\circ$ (i.e., ignoring the aspect sensitivity of the head echo), the pair α and $(\beta + \gamma)$ obtained with our fitting procedure appears to be within the range of values in the solution space that are in closer agreement with those reported by Carrillo-Sánchez et al. (2016; see Figure 10(c)). Note that the coefficient α represents the number of particles contributed by JFCs, and $(\beta + \gamma)$ represents the number of particles from HTC and OCCs. Nevertheless, as mentioned above, this results in our model altitude distribution fitting fairly satisfactorily only in the case for the Arecibo radar. It can be inferred from Figure 10(a) that the number of particles predicted in the altitude distribution by the model is significantly low, especially in the case of PFISR and MU radars. These observations raise questions as to whether the

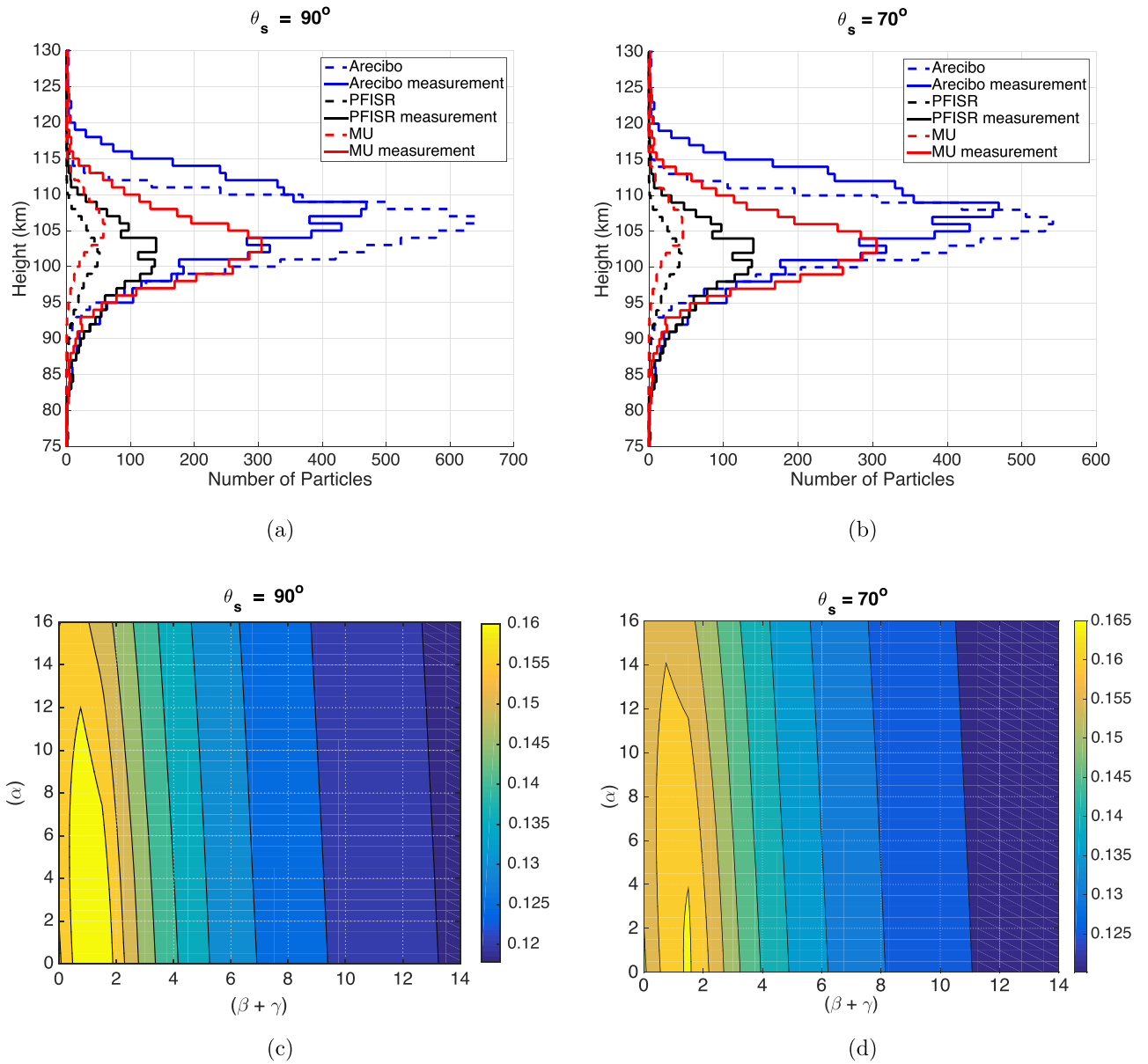


Figure 10. Upper panels: comparison of the fitted modeled and measured altitude distributions simultaneously for the three radars for the cases of $\theta_s = 90^\circ$ and 70° when a head plasma volume size is set to 20% of the mean free path (i.e., $L = 5$). Lower panels: the contour plots for the solution space of α and $(\beta + \gamma)$ for the fitting in which the same pair of α and $(\beta + \gamma)$ was obtained for all three radars simultaneously.

dynamical models underestimate the contributions from the long-period comets and meteors entering Earth’s atmosphere, or if there are effects unaccounted for regarding the ablation and detection of meteors by these radars.

5. Conclusions

In this work, we applied a Monte Carlo simulation technique to model the altitude distributions of meteor head echoes observed by three HPLA radars—Arecibo, PFISR, and MU. These radars differ in sensitivity and/or frequency and thus enable our understanding of the detection of these particles as a function of their physical and dynamical properties to be tested, as well as shed light on any potential biases these measurements may have. We have utilized the updated version of CABMOD for masses in the range of 0.01–1000 μg , entry velocities between 11 and 72 km s^{-1} , and zenith entry angles between 0° and 90° . We also use a simple model of the meteor

head plasma in order to determine the S/N of the detected particles. We first fitted our model to the measurements by each radar system separately and found that our model agrees fairly well for the case of the two UHF radars—Arecibo and PFISR. Notice that, although both radars have the same frequency, their sensitivity to the detected mass range is significantly different. The agreement for these systems provides confidence that overall, the description of the ablation process as well as the S/N treatment is, at least at first order, reasonable. However, for the case of the MU radar, which transmits at VHF frequencies, although our model is able to reproduce the shape of the distribution of the measurement, the peak altitude in the modeled distribution appears to be $\sim 2\text{--}3$ km higher than the measurements. We also investigated the dependence of the results on different radar scatter volume sizes, showing that a radar target volume size of $\text{MFP}/5$ fits reasonably well with the measurements for all three radars, in agreement with the results

reported by Janches et al. (2017). The best-fit ratio for α and $(\beta + \gamma)$ appears to be 0.50:1.00 for the case of the Arecibo radar and 5:80:4.50 for the case of PFISR. Although this ratio may be increased to 5:1 within the 10% confidence level for the case of the Arecibo radar and 3:1 for the case of PFISR, all of these results yield an estimated contribution from JFC meteoroids that is significantly smaller than the expected influx of JFCs from the dynamical models (Nesvorný et al. 2010). Furthermore, Carrillo-Sánchez et al. (2016) required a JFC to long-period comet mass flux ratio of ~ 6 to simultaneously reproduce LIDAR observations of the vertical Na and Fe fluxes above 87.5 km and the measured cosmic spherule accretion rate at the South Pole. We further investigated the potential impact of aspect sensitivity effects on meteor head echo measurements separately for each radar. We found that this effect only affects the detection of small particles, and it increases the predicted contribution of JFCs only for the high-sensitivity Arecibo radar by a factor of 2–3 when the radar scattering becomes aspect-sensitive with $\theta_s < 70^\circ$.

In order to obtain a unique solution for the incoming flux, we performed a fit of our model to the combined measurements obtained with the three radars. We found a solution that results in a number of JFC particles that is in agreement with previous studies. However, the agreement between model and observation is weaker. In particular, for the Arecibo radar, the model overpredicts the observations by 40% while for the case of PFISR and MU, the model underpredicts the observations by 60% and 85%, respectively. This may point to an additional shortcoming with respect to the mass range utilized in our model, as the larger collecting areas of PFISR and MU make them more suitable for detecting particles larger than the particles ($\leq 1000 \mu\text{g}$) utilized in this work. At least a portion of this underprediction may be solved by simply including larger particles. However, the inclusion of these particles is not straightforward, as CABMOD assumes thermal equilibrium across the meteoroid body, which may not be accurate for particles larger than those considered here.

Finally, it is important to note that aside from the free parameters involved in CABMOD and the radar detection model, uncertainties in the dynamical models may be in part also responsible for some of the differences found in this work. Pokorný et al. (2018), using the same dynamical models at Mercury's orbit, showed that results may vary significantly when parameters such as the collisional lifetime of meteoroids in orbit and mass indices at the cometary source are treated as free parameters. It remains to be explored how these results as well as those reported by Carrillo-Sánchez et al. (2016) change if other cases are considered and to what degree this may be one of the causes and why our radar model currently overpredicts the detection of slow particles.

N.S. was supported to perform this work through NSF AGS award #1451241, as well as by the NASA Heliophysics LNAPP, Planetary Astronomy and Solar System Observations Programs; D.J. and P.P. have been supported through the NASA Heliophysics LNAPP, Planetary Astronomy and Solar System Observations Programs; J.D.C.S. and J.M.C.P. were supported by the European Research Council (Project 291332, CODITA). Z.S. was supported through NSF's AGS program. The Arecibo Observatory is operated and managed by the Consortium of the University of Central Florida, Universidad Metropolitana, and Yang Enterprises, under a cooperative

agreement with the National Science Foundation. PFISR is operated by SRI International under a cooperative agreement with the National Science Foundation. The MU radar is operated by RISH, Kyoto University.

ORCID iDs

N. Swarnalingam  <https://orcid.org/0000-0003-4275-8859>

D. Janches  <https://orcid.org/0000-0001-8615-5166>

P. Pokorný  <https://orcid.org/0000-0002-5667-9337>

J. M. C. Plane  <https://orcid.org/0000-0003-3648-6893>

References

- Brown, P., Weryk, R. J., Wong, D. K., & Jones, J. 2008, *Icar*, **195**, 317
- Campbell-Brown, M., & Jones, J. 2003, *MNRAS*, **343**, 775
- Campbell-Brown, M. D., & Close, S. 2007, *MNRAS*, **382**, 1309
- Carrillo-Sánchez, J. D., Nesvorný, D., Pokorný, P., Janches, D., & Plane, J. M. C. 2016, *GeoRL*, **43**, 11
- Chau, J. L., & Woodman, R. F. 2004, *ACPD*, **3**, 6063
- Close, S., Hunt, S. M., Minardi, M. J., & McKeen, F. M. 2000, *RaSc*, **35**, 1233
- Close, S., Oppenheim, M., Hunt, S., & Coster, A. 2004, *Icar*, **168**, 43
- Close, S., Oppenheim, M., Hunt, S., & Dyrud, L. 2002, *JGRA*, **107**, 1295
- Close, S., Volz, R., Loveland, R., et al. 2012, *Icar*, **221**, 300
- Dimant, Y. S., & Oppenheim, M. M. 2017a, *JGRA*, **122**, 4669
- Dimant, Y. S., & Oppenheim, M. M. 2017b, *JGRA*, **122**, 4697
- Dyrud, L., Wilson, D., Boerve, S., et al. 2008, *AdSpR*, **42**, 136
- Fentzke, J. T., & Janches, D. 2008, *JGRA*, **113**, A03304
- Fentzke, J. T., Janches, D., & Sparks, J. J. 2009, *JASTP*, **71**, 653
- Gao, B., & Mathews, J. D. 2015a, *MNRAS*, **446**, 3404
- Gao, B., & Mathews, J. D. 2015b, *MNRAS*, **452**, 4252
- Gómez Martín, J. C., Bones, D. L., Carrillo-Sánchez, J. D., et al. 2017, *ApJ*, **836**, 212
- Grim, E., & Staubach, P. 1996, in ASP Conf. Ser. 104, Dynamic Populations of Dust in Interplanetary Space, IAU Coll. 150: Physics, Chemistry, and Dynamics of Interplanetary Dust, ed. B. A. S. Gustafson & M. S. Hanner (San Francisco, CA: ASP), 3
- Hedin, A. E. 1991, *JGR*, **96**, 1159
- Hocking, W. K., Ruester, R., & Czechowsky, P. 1986, *JATP*, **48**, 131
- James, A. D., Brooke, J. S. A., Mangan, T. P., et al. 2018, *ACP*, **18**, 4519
- Janches, D., Close, S., & Fentzke, J. T. 2008, *Icar*, **193**, 105
- Janches, D., Heinselman, C. J., Chau, J. L., Chandran, A., & Woodman, R. 2006, *JGRA*, **111**, A07317
- Janches, D., Hocking, W., Pifko, S., et al. 2014a, *JGRA*, **119**, 2269
- Janches, D., Mathews, J. D., Meisel, D. D., Getman, V. S., & Zhou, Q.-H. 2000, *Icar*, **143**, 347
- Janches, D., Plane, J. M. C., Nesvorný, D., et al. 2014b, *ApJ*, **796**, 41
- Janches, D., Pokorný, P., Sarantos, M., et al. 2018, *GeoRL*, **45**, 1713
- Janches, D., Swarnalingam, N., Carrillo-Sánchez, J. D., et al. 2017, *ApJ*, **843**, 1
- Janches, D., Swarnalingam, N., Plane, J. M. C., et al. 2015, *ApJ*, **807**, 13
- Jones, J., Brown, P., Ellis, K. J., et al. 2005, *P&SS*, **53**, 413
- Kero, J., Szasz, C., Nakamura, T., et al. 2012, *AnGeo*, **30**, 639
- Kero, J., Szasz, C., Wannberg, G., Pellinen-Wannberg, A., & Westman, A. 2008, *GeoRL*, **35**, L07101
- Marshall, R. A., & Close, S. 2015, *JGRA*, **120**, 5931
- Mathews, J. D. 2004, *JASTP*, **66**, 285
- Mathews, J. D., Janches, D., Meisel, D. D., & Zhou, Q.-H. 2001, *GeoRL*, **28**, 1929
- Mathews, J. D., Meisel, D. D., Hunter, K. P., Getman, V. S., & Zhou, Q. 1997, *Icar*, **126**, 157
- Nesvorný, D., Janches, D., Vokrouhlický, D., et al. 2011a, *ApJ*, **743**, 129
- Nesvorný, D., Jenniskens, P., Levison, H. F., et al. 2010, *ApJ*, **713**, 816
- Nesvorný, D., Vokrouhlický, D., Pokorný, P., & Janches, D. 2011b, *ApJ*, **743**, 37
- Oppenheim, M. M., & Dimant, Y. S. 2015, *GeoRL*, **42**, 681
- Pellinen-Wannberg, A. 2005, *AnGeo*, **23**, 201
- Pellinen-Wannberg, A., & Wannberg, G. 1994, *JGR*, **99**, 11379
- Pifko, S., Janches, D., Close, S., et al. 2013, *Icar*, **223**, 444
- Plane, J., Feng, W., & Dawkins, E. 2003, *ChRv*, **103**, 4963
- Plane, J. M. C. 2004, *ACP*, **4**, 627
- Plane, J. M. C. 2012, *ChSRv*, **41**, 6507
- Pokorný, P., Sarantos, M., & Janches, D. 2018, *ApJ*, **863**, 31
- Pokorný, P., Vokrouhlický, D., Nesvorný, D., Campbell-Brown, M., & Brown, P. 2014, *ApJ*, **789**, 25

- Popova, O. P., Strelkov, A. S., & Sidneva, S. N. 2007, [AdSpR](#), **39**, 567
- Rapp, M., & Lübken, F.-J. 2004, [ACP](#), **4**, 2601
- Rowan-Robinson, M., & May, B. 2013, [MNRAS](#), **429**, 2894
- Schult, C., Stober, G., Chau, J. L., & Latteck, R. 2013, [AnGeo](#), **31**, 1843
- Schult, C., Stober, G., Janches, D., & Chau, J. L. 2017, [Icar](#), **297**, 1
- Sparks, J. J., & Janches, D. 2009a, [GeoRL](#), **36**, L17101
- Sparks, J. J., & Janches, D. 2009b, [GeoRL](#), **36**, L12105
- Subasinghe, D., Campbell-Brown, M. D., & Stokan, E. 2016, [MNRAS](#), **457**, 1289
- Swarnalingam, N., Hocking, W. K., & Argall, P. S. 2009, [AnGeo](#), **27**, 1643
- Swarnalingam, N., Hocking, W. K., & Drummond, J. R. 2011, [JASTP](#), **73**, 957
- Thomas, E., Horányi, M., Janches, D., et al. 2016, [GeoRL](#), **43**, 3645
- Voigt, C., Schlager, H., Luo, B. P., et al. 2005, [ACP](#), **5**, 1371
- Vondrak, T., Plane, J. M. C., Broadley, S., & Janches, D. 2008, [ACP](#), **8**, 7015
- Westman, A., Wannberg, G., & Pellinen-Wannberg, A. 2004, [AnGeo](#), **22**, 1575
- Yang, H., & Ishiguro, M. 2015, [ApJ](#), **813**, 87